Pergamon

PII: S0968-4328(97)00056-5

Micron Vol. 29, No. 2/3, pp. 191–199, 1998
Published by Elsevier Science Ltd
Printed in Great Britain
0968-4328/98 $19.00+0.00

High-spatial Resolution Compositionally-sensitive Imaging of Metallic Particles using Plasmon Energy-loss Electrons in TEM

EDEN M. HUNT,* ZHONG LIN WANG,* NEAL D. EVANS† and JANET M. HAMPIKIAN*‡

**School of Materials Science and Engineering, Georgia Institute of Technology, Atlanta, GA 30332-0245, U.S.A.*
†Oak Ridge Institute for Science and Education, P.O. Box 117, Oak Ridge, TN 37831-0117, U.S.A.

(*Received* 27 *February* 1997; *accepted* 29 *August* 1997)

Abstract—High spatial resolution elemental maps have been demonstrated in studies of Y^+ implanted alumina and Al/Ti multilayer specimens using energy-filtered transmission electron microscopy. A spatial resolution of ~2 nm is achieved. Aluminum containing particles formed in Y^+ implanted alumina have been identified using energy-filtered images formed with plasmon energy-loss electrons. Noncrystalline aluminum containing particles in specimens implanted at lower ion energies are also observed and the image contrast can be reasonably interpreted using a compositional shell model. Published by Elsevier Science Ltd

Key words: energy-filtering, aluminum, alumina, plasmon, compositionally sensitive imaging, spatial resolution.

INTRODUCTION

Many materials problems are closely related to the compositions of the phases present in the system. Although crystal lattices can be determined reasonably well using high-resolution electron microscopy, determination of local chemistry, particularly at high spatial-resolution, remains a rigorous challenge. Quantitative compositional imaging is vitally important for characterizing advanced materials. Most chemical imaging is performed using scanning electron microscopy (SEM) and scanning transmission electron microscopy (STEM). In STEM, the electron beam from a field emission gun is focused onto the surface of the specimen using a condenser lens, and the beam is scanned over the specimen with the use of deflection coils. Characteristic inelastic scattering signals emitted from the interaction volume of the electron probe with the specimen are determined by the thickness-projected elemental concentrations, provided there is no beam broadening or fluctuation in incident beam current. The detected inelastic scattering signals at each beam scanning position are displayed on a phosphor screen producing a contrast pattern which is an approximate representation of the chemical positions in the specimen. The interaction of an incident electron with the specimen also causes the emission of X-rays, Auger electrons and secondary electrons. X-rays and Auger signals are used extensively to obtain chemical information from the volume and the surface of a specimen, respectively, and the secondary electron signal allows surface morphology to be imaged in both SEM and STEM.

The energy-filtering system developed in recent years has made it possible to perform chemically sensitive imaging in a transmission electron microscope (TEM) (Reimer, 1995). Characteristic inelastic signals observed in electron energy-loss spectra provide fingerprints of the elements present in the specimen. By separating the electrons with different energy-losses at the exit face of an electron energy-loss spectrometer (EELS), and introducing an energy-selecting system that allows only the electrons with a specific energy-loss to pass through the imaging system, and finally re-dispersing the electrons with a set of magnetic lenses in correspondence to the real space distribution, compositionally sensitive images may be obtained (Reimer *et al.*, 1990; Shuman *et al.*, 1986; Krivanek *et al.*, 1995; Craven and Colliex, 1977). Compositionally sensitive imaging, in general, relies on the signal of the inner shell ionization edge, the intensity of which is largely affected by the threshold energy-loss and the ionization cross-section of the edge. Therefore, the spatial resolution of the image is strongly affected by the signal-to-noise ratio (Wang and Shapiro, 1995). In this respect, lower loss electrons from the plasmon or valence region of the energy loss spectrum (10–100 eV) are favourable for this type of imaging due to the much higher signal intensity, provided any delocalization effects are small in comparison to the required spatial resolution.

In this paper, compositionally sensitive imaging using plasmon energy-loss electrons is explored for a special case in which nanoscale particles are present in an amorphous substrate, and for an atomically sharp Al/Ti interface. It will be shown that the energy filtering system is uniquely capable of imaging and identifying the nature of the particles. A spatial resolution better than 2 nm can be achieved.

‡Corresponding author.

EXPERIMENTAL METHODS

Single crystal alumina (–1–123) was ion implanted at ambient temperature with either 100 or 170 keV singly charged yttrium ions to a fluence of 5×10^{16} ions/cm^2. Planar view specimens were prepared for TEM observations using standard dimple grinding and ion beam milling techniques. Energy filtered transmission electron microscopy experiments were performed with a Gatan Imaging Filter (GIF™) interfaced to a Philips CM30 TEM operated at 300 kV. The low-loss images were gain normalized, 512×512 pixels in size and were recorded with an exposure time of 1 s and an energy-selecting window of 5 eV. Images acquired using core-loss electrons were recorded with an exposure time of 30 s and an energy-selecting window of 30 eV. Additional information was obtained by electron diffraction, bright field imaging and energy dispersive X-ray spectroscopy with an oxygen sensitive detector in a Hitachi HF-2000 TEM operated at 200 kV.

Al/Ti polycrystalline multilayer specimens were prepared by sputtering as described in detail elsewhere (Shechtman *et al.*, 1994). Cross-sectional TEM specimens were prepared which provided atomically sharp, epitaxial interfaces. The Al/Ti specimen was imaged using a JEOL 3010 TEM at 300 kV equipped with a GIF system. Some of the EELS spectra were acquired using a Hitachi HF-2000 TEM operated at 200 kV.

COMPOSITIONALLY SENSITIVE IMAGING

The first specimen examined was single crystal alumina implanted at ambient temperature with 100 keV Y^+ to a fluence of 5×10^{16} ions/cm^2. Ion channelling, Knoop microhardness measurements, and transmission electron microscopy (TEM) all indicate that the alumina surface layer was amorphized by the implantation (Hunt *et al.*, 1996a, 1996b; Hunt and Hampikian, 1997). Bright field TEM revealed a lack of diffraction contrast in this sample and displayed only a diffuse electron diffraction haze associated with the presence of an amorphous phase. However, an optical absorption feature in the near ultraviolet indicated the presence of nanostructures in this sample. For this reason energy-filtered imaging was carried out in order to image these nanostructures (Evans *et al.*, 1995). Before presenting the energy-filtered images an understanding of the valence/plasmon electron energy loss patterns of the elements involved is instructive. Single-scattering energy-loss spectra from standard specimens (Ahn and Krivanek, 1983) of alumina (Al_2O_3), aluminum (Al) and yttria (Y_2O_3) are shown in Fig. 1; these are all possible components of this system. The strong peak at about 38 eV is the Y–$N_{2,3}$ ionization edge. Both the Al and Y_2O_3 spectra show a loss feature at 15 eV and the Al_2O_3 spectrum has a broad feature centered at approximately 24 eV. A typical energy loss spectrum from one of the yttrium implanted alumina samples is also shown in Fig. 1. This spectrum, which is offset along the y-axis for ease of viewing, contains both the broad Al_2O_3 feature at 24 eV and the sharper peak at 15 eV. This comparison of spectra indicates that energy-filtered images formed using the electrons with energy-losses of 15 eV, 25 eV and 40 eV may yield information about the chemical nature of the nanostructures formed during this ion implantation.

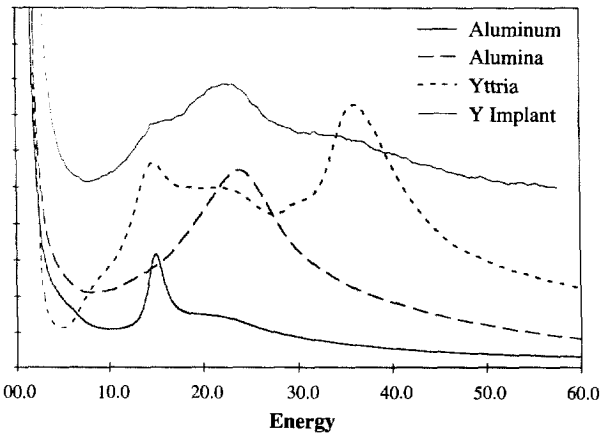

Fig. 1. A comparison of EELS spectra acquired from an aluminum foil, alumina, yttria and a yttrium implanted alumina sample for selecting the characteristic peaks which might be used for forming energy-filtered images. The implanted sample spectrum has been offset along the y-axis for clarity.

A zero-loss electron image of an implanted area is shown in Fig. 2(a). In this image the particles present in the sample are not apparent and the gradual contrast variation is due to the increasing thickness of the sample. Imaging with 15 eV energy-loss electrons (Fig. 2(b)), using a 5 eV energy window, revealed particles within in the alumina matrix. These particles have sizes which range from 20–100 nm. A striking phenomenon is the fine 4–10 nm substructure within the particles, possibly indicating compositional gradients within the particles. In the image formed by the 25 eV energy-loss electrons (Fig. 2(c)), the bright features (particles) observed in Fig. 2(b) are darker than the surrounding matrix. This result indicates that these particles are not composed of alumina. In addition, the image recorded using the 40 eV energy-loss electrons (Fig. 2(d)) also shows the particles with a lower intensity than the surrounding matrix material. As discussed above, the 38 eV edge is only present in the spectrum of Y_2O_3, thus, this image confirms that the particles are not yttria. All of these images support the conclusion that these particles are neither alumina nor yttria.

Similar investigations on another specimen which was implanted with 170 keV Y^+ to a fluence of 5×10^{16} ions/cm^2 resulted in comparable images. The zero-loss filtered image (Fig. 3(a)) shows very weak contrast from some of the crystalline particles contained in this sample. The 25 eV loss image (Fig. 3(c)) demonstrates that these particles are not alumina, while the image recorded from the 15 eV energy-loss electrons (Fig. 3(b)) shows many more particles than are apparent in the other images. This is in agreement with the observations shown in

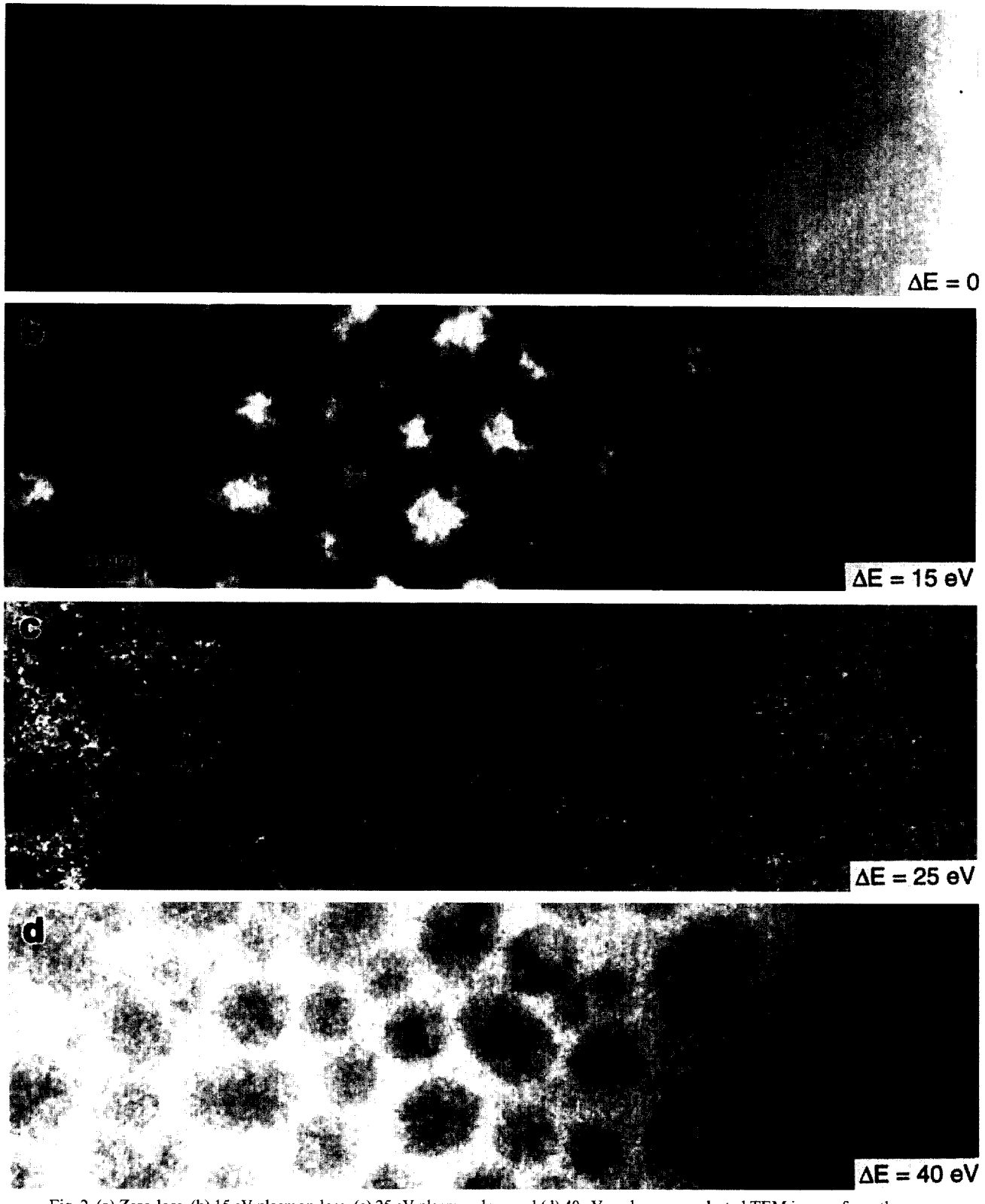

Fig. 2. (a) Zero-loss, (b) 15 eV plasmon-loss, (c) 25 eV plasmon-loss and (d) 40 eV peak energy-selected TEM images from the same specimen region of a 100 keV Y^+ implanted alumina specimen. The energy selection window was centered at these energies specified and its width was 5 eV.

Fig. 2, with the exception that these particles demonstrate little or no substructure. The particle sizes are in the range of 10–15 nm, much smaller than those shown in Fig. 2, despite being the result of the implantation of an identical amount of yttrium (5×10^{16} ions/cm^2). An oxygen 'jump-ratio' image (post O–K edge divided by pre O–K edge) from the same area (Fig. 3(d)) shows that the particles are deficient in oxygen with respect to the surrounding matrix material. This result also agrees with previous energy dispersive X-ray spectroscopy (EDS)

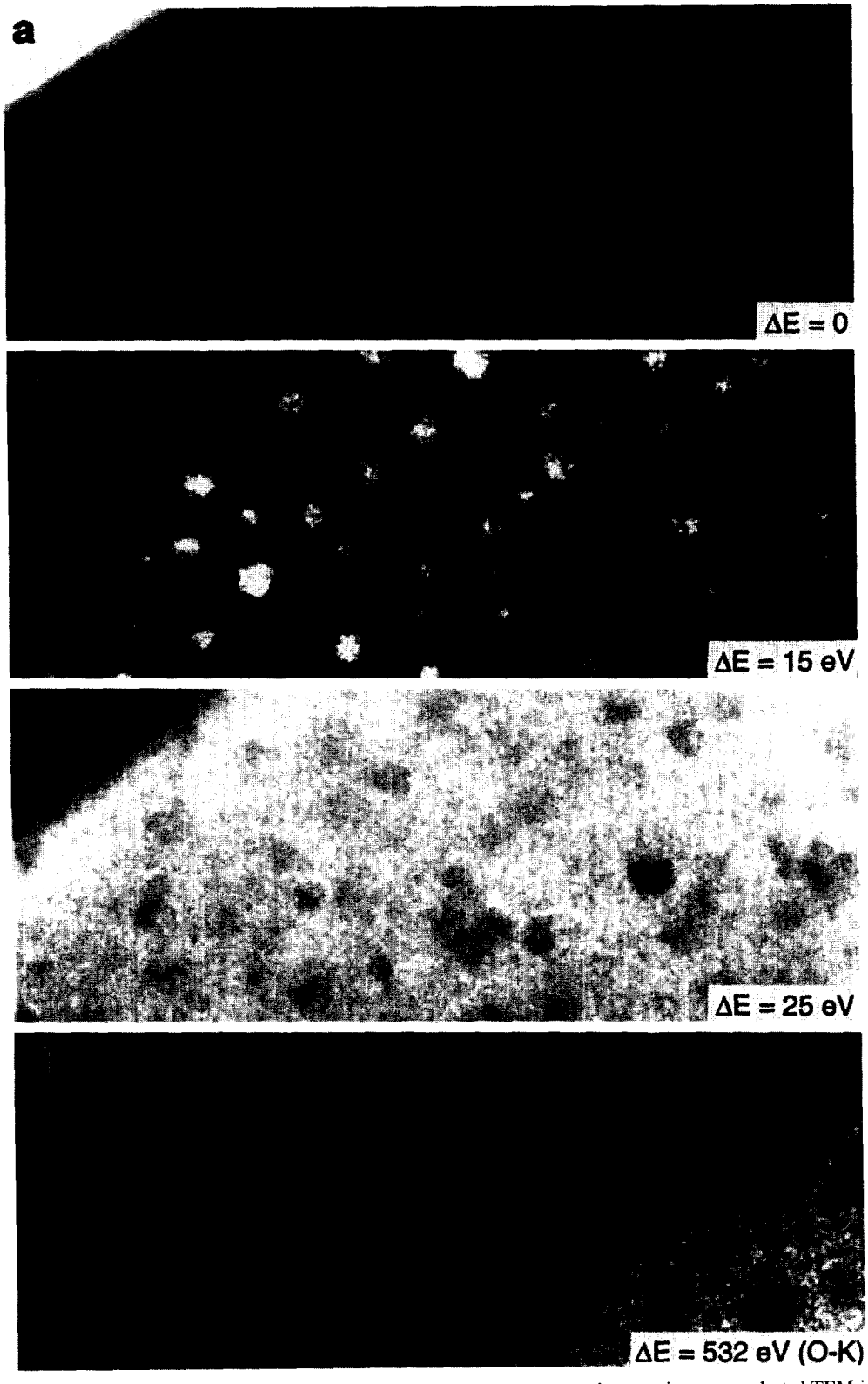

Fig. 3. (a) Zero-loss, (b) 15 eV plasmon-loss, (c) 25 eV plasmon-loss and (d) oxygen jump ratio energy-selected TEM images from the same specimen region of a 170 keV Y^+ implanted alumina specimen. The energy selection window was centered at these energies specified and its width was 5 eV.

analysis which showed that the particles are oxygen deficient with respect to the matrix material (Hunt *et al.* 1996a, 1996b; Hunt and Hampikian, 1997).

To finalize our identification of the nature of the observed particles, EELS spectra were acquired using electrons transmitted through the particles, the matrix and a standard thin film specimen of Al with surface oxidation, as shown in Fig. 4(a). It is apparent that the 15 eV peak observed in the spectrum from the particle bearing region agrees well with the volume plasmon peak of metallic Al, and there is no detectable metallic Al in the matrix. The 25 eV peak observed in the

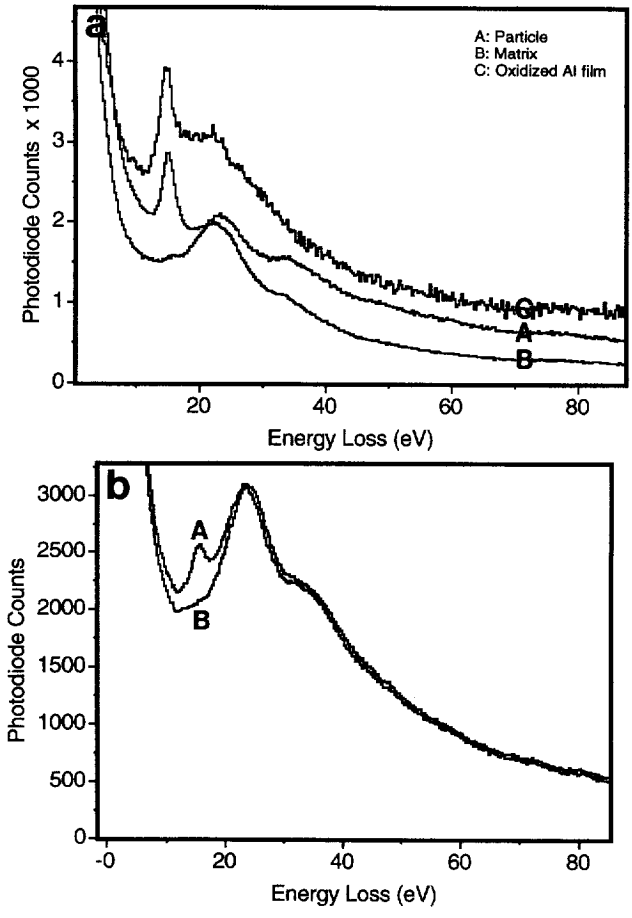

Fig. 4. Energy-loss spectra from (A) an embedded particle and (B) the adjacent amorphous matrix for (a) a large particle and (b) a small particle, where the spectrum C was acquired from a standard thin Al foil covered by alumina oxidation layers.

standard Al specimen is due to the volume excitation of the unavoidable alumina oxidation layer at the top and bottom surfaces of the metal film. The spectra from the embedded particle and the oxidized Al standard are quite similar in major characteristics, allowing the conclusion that the observed particles are metallic Al. Fig. 4(b) shows a comparison of two spectra acquired from a small size ($\sim$5 nm) particle and its adjacent matrix. The intensity of the 15 eV peak in the particle's spectrum is significantly reduced due to the smaller particle size which results in a decrease in the amount of thickness-projected metallic Al in the beam illumination region.

The particles formed in the alumina matrix implanted with 170 keV Y^+ clearly show solid contrast with no substructure. In addition, these particles are crystalline. Electron diffraction patterns recorded from a large area have been used to determine the lattice constant of the particle material, with the aid of a standard Au diffraction pattern recorded under the same imaging conditions. The particles have an FCC structure with a lattice parameter of a=0.411 $\pm$ 0.002 nm (Fig. 5(a)). High resolution lattice images of the particles were used to carry out an independent calculation of the lattice parameter (Fig. 5(b)). The particle in Fig. 5 is oriented along [011], and the lattice parameter a=0.41 nm $\pm$ 0.03 nm, is in good agreement with the diffraction measurements. Therefore, the similarity between the particle crystallography and that of pure aluminum (which is FCC with a lattice parameter of 0.404 nm), in conjunction with the EFTEM results suggests that the particles are metallic aluminum nanocrystals with a slightly dilated lattice parameter, possibly due to the incorporation of a small amount of yttrium.

SPATIAL RESOLUTION

As observed in Fig. 2, the Al-rich particles show contrast suggestive of compositional gradients present in the particles. To estimate the optimum spatial resolution that can be achieved using plasmon energy-loss electrons, image processing is carried out. This processing consists of subtracting the contribution of the alumina matrix from the 15 eV-loss image. This contribution was estimated using adjacent loss images and subtracted from the original 15 eV-loss image (Evans *et al.*, 1995). Fig. 6(a) shows a processed 15 eV energy-filtered image from the specimen implanted with 100 keV Y^+. A line scan across a particle (indicated by a line in Fig. 6(a)) is shown in Fig. 6(b). This line scan contains two peaks representing the intensity of the particle image along the indicated line. The full width at half maximum of this intensity is measured to be W=3.7 $\pm$ 0.3 nm. This value includes not only the finite width of the Al wall but also the contrast blurring due to the delocalization effect in plasmon excitation.

In this implanted sample both the particles and the surrounding matrix are amorphous, therefore it is difficult to use conventional imaging or diffraction techniques to estimate the local thickness of the Al substructure present in these particles. Therefore, another specimen with a known interface structure was used to determine the spatial resolution that can be expected using 15 eV loss electrons. In practice, it is impossible to preserve a metallic Al surface without oxidation in conventional TEM with a vacuum of 10^{-7}–10^{-8} Torr in the column. The interface studies were carried out using a cross-sectional Ti/Al multilayer sample. Fig. 7(a) and (b) show a pair of high-resolution lattice images of an Al/Ti (111) interface recorded using zero-loss and Al plasmon-loss electrons, respectively. The Al/Ti interface is atomically sharp and is oriented parallel to the incident beam direction. It is apparent that the crystal lattice fringes are resolved in the image recorded using the inelastically scattered electrons. The overall contrast of the plasmon-loss energy-selected image may provide compositionally sensitive information, but the lattice fringes are still governed by phase contrast (Wang, 1997), as in conventional HRTEM. Therefore, the bright fringes do not necessarily represent the Al (or Ti) atomic planes.

To estimate the spatial resolution of the plasmon-loss electron image, a line scan is made across the Al/Ti interface, and the result is shown in Fig. 7(c). The fine oscillation in the intensity profile is due to the lattice fringes. The intensity profile drops within a distance of

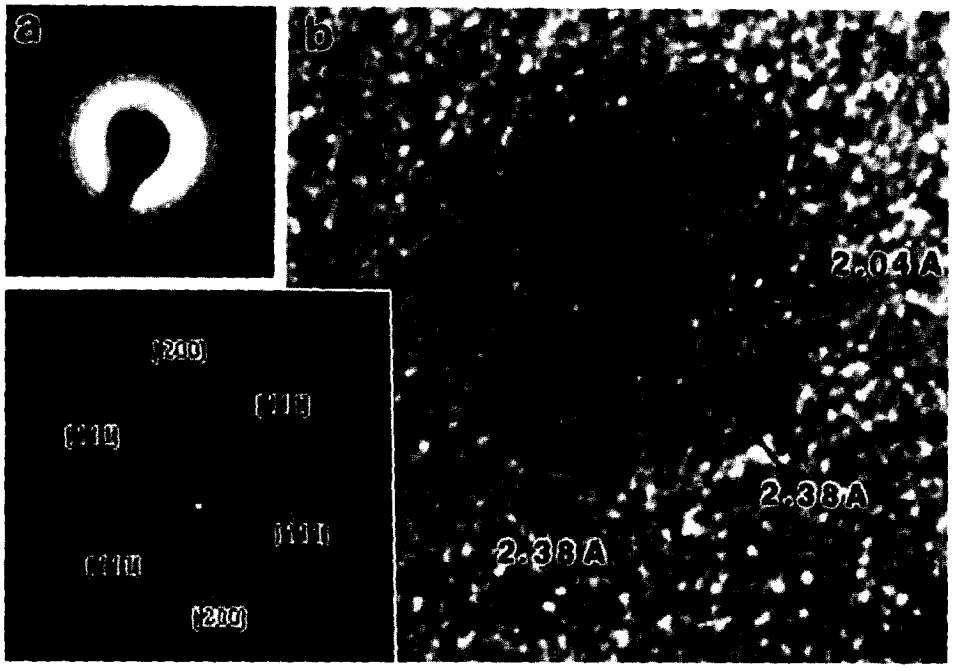

Fig. 5. (a) A selected area electron diffraction pattern and (b) a high-resolution TEM image of a single solid particle from a 170 keV Y^+ implanted alumina specimen.

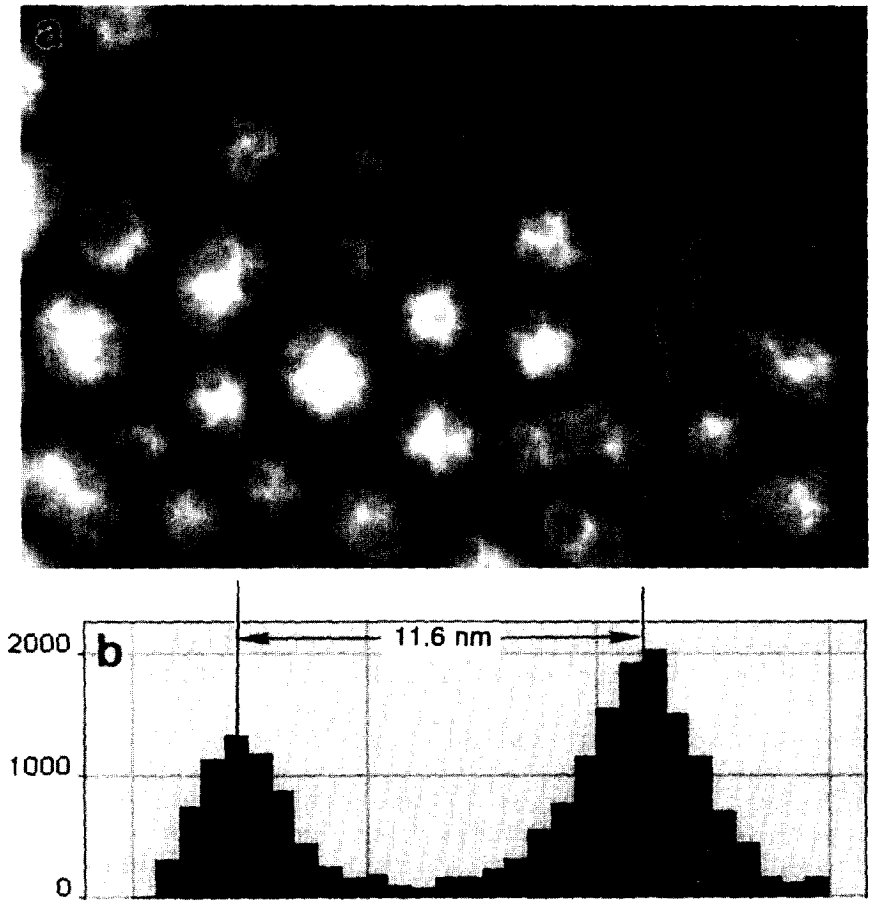

Fig. 6. (a) A background subtracted 15 eV plasmon-loss energy-filtered TEM image showing only the contribution of the metallic Al (b) A line scan across particle A (indicated in (a)) for the estimation of the thickness of the Al wall.

3 nm around the interface. Thus, the spatial resolution is approximately $r_j \approx 1.5$ to 1.8 nm. This spatial resolution is determined by the non-localized scattering of valence electrons (Wang and Shapiro, 1995). Using this value, the thickness of the Al structure in the particles shown in Fig. 6(b) is estimated to be $\Delta d \approx W - r_i \approx 2.1 \pm 0.4$ nm.

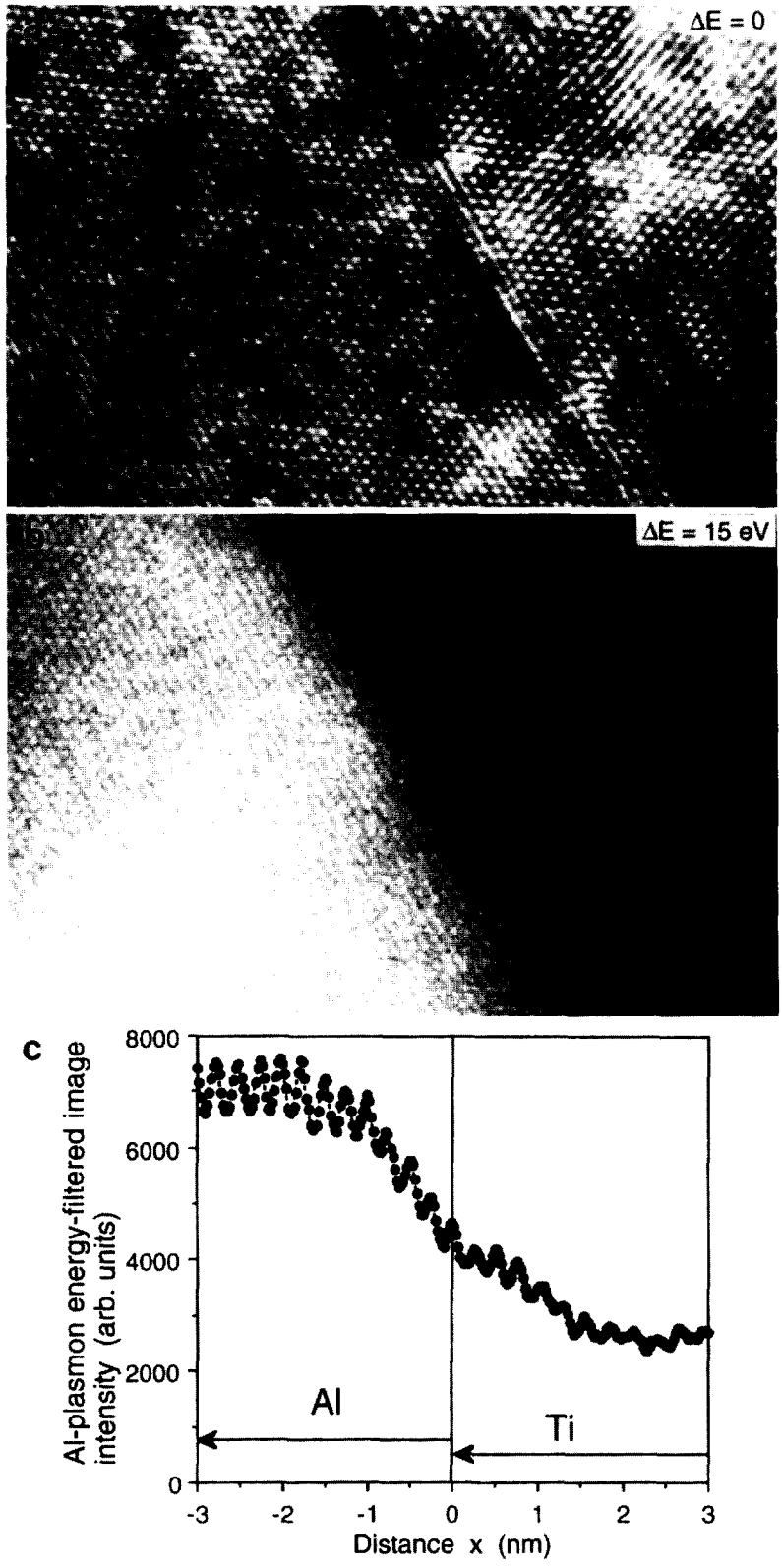

Fig. 7. (a) Zero-loss and (b) 15 eV Al-plasmon loss energy-selected HREM images of an edge-on Al/Ti (111) interface. Energy window Δ=4 eV [10]. (c) An intensity line scan across the Al/Ti interface from the image recorded using the 15 eV Al–plasmon-loss electron image. This curve determines the spatial resolution of valence-loss electron imaging, provided the interface is atomically sharp and there is no interdiffusion.

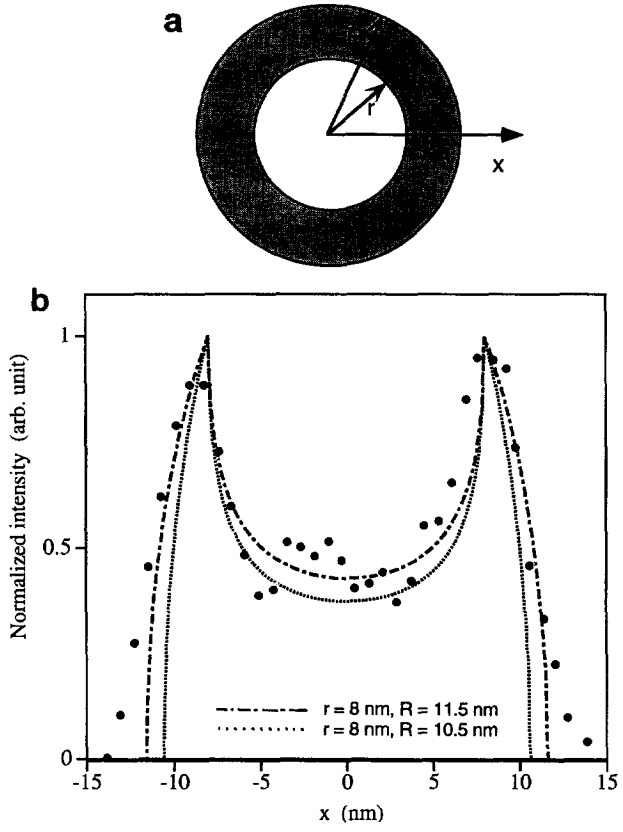

Fig. 8. (a) A spherical shell model of a compositionally porous Al particle, and (b) the projected atom density of the shell particle along the beam direction for two cases in comparison with the experimentally observed profile obtained from the particle B in Fig. 6(a).

DISCUSSION

Thickness projected Al profile across a shell particle

The formation of metallic particles in an alumina matrix is not surprising. This has been observed previously in electron beam induced reduction of alumina in STEM and TEM (Humphreys *et al.*, 1985; Wang, 1991). The reduction mechanism in that study was determined to be an internal Auger decay process for the electron stimulated surface desorption (Feibelman and Knotek, 1978). However, in this study, the incident beam is Y^+ rather than electrons. The mechanism for this Al particle formation is under investigation.

As shown previously in Figs 2 and 6, the Al in the particles shows a sort of porosity or compositional substructure, and some particles, as indicated with A and B in Fig. 6(a), show a single shell shape. If metallic Al is distributed in a shell, as defined by an inner and outer radii (Fig. 8(a)), the projected atom density can be calculated across the particle for various radii (dotted and dashed lines in Fig. 8(b)). The two calculated curves are normalized at $x=r$ for comparing the change in line scan profiles. An experimentally observed line scan intensity is also plotted. It appears that the best fit is obtained for the case with $r=8$ nm and $R=11.5$ nm. On the other hand, with consideration of the broadening of the profile by the finite resolution of the plasmon energy-loss electron, a 1 nm width should be subtracted approximately from the outer radius. A calculation for $r=8$ nm and $R=10.5$ nm is given in Fig. 8(b). Therefore, the thickness of the shell at the intersection of the line scan is $\Delta d=R-r=2.5$ nm, which is in good agreement with the estimation given above (2.1 ± 0.4 nm).

Surface/interface plasmon

Since our experiments were performed by choosing a 5 eV width energy window centered at 15 eV, one might wonder about the contribution from the interface plasmon peak. If we assume the particle is sufficiently large, the energy of the Al-alumina interface plasmon (Wang, 1996) is located at

$$\omega_i=\frac{\omega_p}{\sqrt{\varepsilon+1}}, \tag{1}$$

where the dielectric constant ε of alumina is approximately 9, and the volume plasmon energy $h\omega_p$ of Al is 15 eV. Thus, the interface plasmon energy is $h\omega_i\approx4.7$ eV, falling well outside of the energy-selection window. Therefore, the energy-filtered images are formed only by the volume plasmon excitation.

CONCLUSIONS

In this paper, high spatial resolution, chemically sensitive images have been demonstrated in studies of Y^+ implanted alumina and Al/Ti multilayer specimens using transmission electron microscopy with an electron energy-filtering system. Aluminum particles formed in Y^+ implanted alumina have been identified using the energy-filtered electron images of plasmon energy-losses and electron energy-loss spectra. A spatial resolution of ~2 nm is achieved. Crystalline Al particles are formed in alumina implanted at 170 keV, while larger compositionally porous amorphous Al particles are formed in specimens implanted at 100 keV. The plasmon energy-loss electron image of the porous Al particles can be reasonably interpreted using a compositional shell model.

Acknowledgements—This material is based upon the work supported by the National Science Foundation under grant No. DMR-9624927, by the Division of Materials Sciences, U.S. Department of Energy, under contract DE-AC05-96OR22464 with Lockheed Martin Energy Research Corporation, through the SHaRE Program under the contract DE-AC05-76OR00033 with Oak Ridge Associated Universities, and by the Office of Naval Research through the Molecular Design Institute at Georgia Institute of Technology.

REFERENCES

Ahn, C. C. and Krivanek, O. L., 1983. EELS Atlas. Gatan Inc., Warrendale, PA; and Arizona State University.

Craven, A. J. and Colliex, C., 1977. High resolution energy filtered images in STEM. *J. Microsc. Spectrosc. Electron.*, **2**, 511–522.

Evans, N. D., Bentley, J. and Zinkle, S. J., 1995. Energy-filtered plasmon images of $MgAl_2O_4$ implanted with Al^+ and Mg^+ ions. In *Proc. Microscopy and Microanalysis*, pp. 266–267.

Feibelman, P. J. and Knotek, M. L., 1978. Reinterpretation of electron-stimulated desorption data from chemisorption systems. *Phys. Rev. B*, **18,** 6531–6539.

Humphreys, C. J., Salisbury, I. G., Berger, S. D., Timsit, R. S. and Mochel, M. E., 1985. Nanometre-scale electron beam lithography. In *Inst. Phys. Conf. Ser. No. 78*, Ch. 1, pp. 1–6. EMAG'85, Newcastle.

Hunt, E. M. and Hampikian, J. M., 1997. Formation and thermal stability of aluminum nanoparticles sythesized via ion implantation into sapphire. *Journal of Materials Science*, accepted 30 October, 1996, in press.

Hunt, E. M., Hampikian, J. M. and Poker, D. B., 1996. Nanocrystal formation via yttrium ion implantation into sapphire. *Mater. Res. Soc. Symp. Proc.*, **396,** 403–410.

Hunt, E. M., Hampikian, J. M. and Evans, N. D., 1996b. The examination of yttrium ion implantated alumina with energy-filtered transmission electron microscopy. In *Proc. Microscopy and Microanalysis*, pp. 534–535.

Krivanek, O. L., Gubbens, A. J. and Dellby, N., 1995. Spatial resolution in EFTEM elemental maps. *J. Microsc.*, **180,** 277–287.

Reimer, L. (ed), 1995. *Energy-Filtering Transmission Electron Microscopy, Springer Series in Optical Sciences*. Springer-Verlag, Berlin, Heidelberg, New York.

Reimer, L., Bakenfelder, A., Fromm, I., Rennekamp, R. and Ross-Messemer, M., 1990. Electron spectroscopic imaging and diffraction. *Electron Microsc. Soc. Am. Bull.*, **20,** 73–80.

Shechtman, D., Van Heerden, D. and Josell, D., 1994. FCC titanium in Ti–Al multilayers. *Mater. Lett.*, **205/6,** 329–334.

Shuman, H., Chang, C. F. and Somlyo, A. P., 1986. Elemental imaging and resolution in energy-filtered conventional electron microscopy. *Ultramicroscopy*, **19,** 121–134.

Wang, Z. L., 1997. Lattice imaging using plasmon energy-loss electrons. *Ultramicroscopy*, in press.

Wang, Z. L., 1996. Valence electron excitation and plasmon oscillations in thin films, surfaces, interfaces and small particles. *Micron*, **27,** 265–299.

Wang, Z. L., 1991. Reflection electron imaging and spectroscopy studies of metal reduction at alpha-alumina $(0,-1,2)$ surfaces. *J. Microscopy*, **163,** 261–274.

Wang, Z. L. and Shapiro, A. J., 1995. Energy-filtering and compositional imaging in surface and interface studies using HREM. *Ultramicroscopy*, **60,** 115–135.